

Electrical Breakdown of Suspended Mono- and Few-Layer Tungsten Disulfide *via* Sulfur Depletion Identified by *In-Situ* Atomic Imaging

Ye Fan^{1†}, Alex W. Robertson^{1,2*†}, Yingqiu Zhou¹, Qu Chen,¹ Xiaowei Zhang³, Nigel D. Browning^{2,4},
Haimei Zheng³, Mark H. Rümmeli⁵, Jamie H. Warner^{1*}

¹Department of Materials, University of Oxford, Parks Road, Oxford, OX1 3PH, United Kingdom

²Physical & Computational Science Directorate, Pacific Northwest National Laboratory, Richland, WA
99352 United States

³Materials Sciences Division, Lawrence Berkeley National Laboratory, Berkeley, California 94720,
United States

⁴Department of Materials Science and Engineering, University of Washington, Seattle, WA 98195,
United States

⁵Soochow Institute for Energy and Materials Innovations, College of Physics, Optoelectronics and
Energy, Collaborative Innovation Center of Suzhou Nano Science and Technology, Key Laboratory of
Advanced Carbon Materials and Wearable Energy Technologies of Jiangsu Province, Soochow
University, Suzhou 215006, China

⁶Centre of Polymer and Carbon Materials, Polish Academy of Sciences, M. Curie-Skłodowskiej 34,
Zabrze 41-819, Poland

*alex.w.robertson@gmail.com; jamie.warner@materials.ox.ac.uk

KEYWORD: WS₂, 2D dichalcogenides, TEM, *in situ*, electrical breakdown

ABSTRACT: The high-bias and breakdown behavior of suspended mono- and few-layer WS₂ was explored by *in situ* aberration corrected transmission electron microscopy (AC-TEM). The suspended WS₂ devices were found to undergo irreversible breakdown at sufficiently high biases due to vaporization of the WS₂. Simultaneous to the removal of WS₂ was the accompanying formation of few-layer graphene decorated with W and WS₂ nanoparticles, with the carbon source attributed to organic residues present on the WS₂ surface. The breakdown of few-layer WS₂ resulted in the formation of faceted S-depleted WS₂ tendrils along the vaporization boundary, which were found to exhibit lattice contraction indicative of S depletion, alongside pure W phases incorporated into the structure, with the interfaces imaged at atomic resolution. The combination of observing the graphitization of the amorphous carbon surface residue, W nanoparticles, and S depleted WS₂ phases following the high-bias WS₂ disintegration all indicate a thermal Joule heating breakdown mechanism over an avalanche process, with WS₂ destruction promoted by preferential S emission. The observation of graphene formation, and the role the thin amorphous carbon layer has in the pre-breakdown behavior of the device, demonstrate the importance of employing encapsulated heterostructure device architectures that exclude residues.

The exploitation of semiconducting two-dimensional materials is necessary for the realization of electronic and optoelectronic devices at the limit of miniaturization, offering advantages in power efficiency, device density, and transparency.¹ Such devices require a semiconducting material with a direct band gap within the optical window. Monolayer metal dichalcogenides exhibit this electronic structure, and thus have been the subject of intensive research.^{2–5} Understanding the limitations and deficiencies of these materials is necessary for informed device fabrication, including knowledge of both the fundamental properties and also the deficiencies that inevitably arise through limitations in synthesis and fabrication capability. The metal-semiconductor interface, semiconductor-substrate interaction, and doping control are among such deficiencies recognized to be precluding the use of two-dimensional materials in electronics applications.⁶

The electrical breakdown of semiconductors is one such fundamental limit, with it leading to potentially irreversible material failure that severely alters the behavior of the device. The specifics of the breakdown process can vary significantly depending on the material, device, and conditions; it can be the result of

either thermal or electrical mechanisms, and might proceed through an intermediate reversible phase (soft breakdown) prior to complete failure (hard breakdown).⁷⁻⁹ Common through all is that they are ultimately instigated through the application of a high electric field. For two-dimensional materials we must consider two distinct scenarios; breakdown with an electric field parallel or orthogonal to the basal plane of the sheet. For materials to be used as a dielectric layer, for instance in all-2D heterostructures, understanding the breakdown resulting from gating fields orthogonal to the layer is desirable. A detailed study of the breakdown of the dielectric layered material boron nitride was performed by Hattori *et al.* through conductive AFM.¹⁰ With semiconducting materials it is useful to determine the effect of parallel source-drain fields, where pushing the limit of the material properties can reveal the maximum reversible current density obtainable.¹¹⁻¹³

The distinct morphology of two-dimensional materials presents a departure in the expected behavior upon breakdown, as the extreme thinness ensures that dependences on substrate interaction, surface impurities, and crystal defects will play a large role. Here, we study the electrical breakdown of suspended mono- and few-layer WS₂, and show that following breakdown of the suspended WS₂ a rapid increase in current density is observed, attributed to the simultaneous crystallization of graphene layers from surface residues. This process is tracked *in-situ* at the atomic level using aberration corrected transmission electron microscopy (AC-TEM) combined with an electrical biasing holder. During the WS₂ breakdown, the Joule heating induces crystallization of residual amorphous carbon on the WS₂ surface into graphene, which is also decorated with W and WS₂ nanoparticle remnants of WS₂ breakdown and disintegration. The extreme high bias environment leading to the WS₂ disintegration was found to permit the formation of sulfur depleted phases, with interfaces between these phases imaged at atomic resolution.

Results and Discussion

WS₂ was prepared by chemical vapor deposition (CVD) according to our established recipes (see Methods).^{14,15} The grown crystals were characterized by SEM, Raman spectroscopy, and photoluminescence (PL) spectroscopy (Figure 1a and b, Figure S1), with PL spectroscopy delineating the formation of WS₂ monolayers from few-layers due to the observation of direct-gap enabled luminescence in the monolayer case (Figure 1b).¹⁶ The WS₂ was subsequently transferred to pre-patterned custom-made

silicon nitride membrane chips for *in-situ* TEM (Figure 1c-e).¹⁷ AC-TEM imaging was performed using Oxford's JEOL 2200MCO at a low accelerating voltage of 80 kV to minimize electron beam induced knock-on damage to the sample. The electron beam was blanked while bias sweeps were performed to insure that electrical effects were purely a function of biasing and not beam damage. Imaging at high magnifications prior to breakdown was minimized to prevent beam induced defects and holes leading to premature device failure.

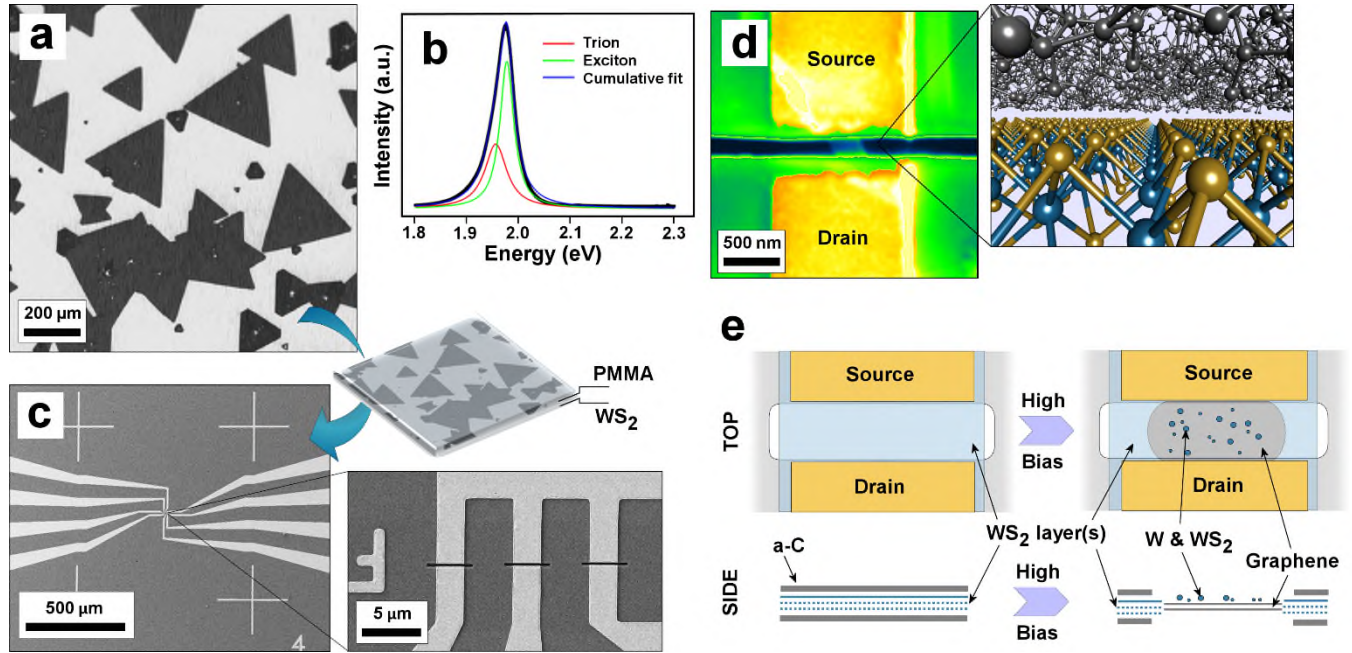


Figure 1. (a) SEM image of CVD synthesized monolayer WS₂ grains grown on a silicon substrate. (b) Photoluminescence spectroscopy of the grown monolayer WS₂ grains. (c) SEM images of the patterned silicon-silicon nitride device substrate to which grown WS₂ was transferred. Magnified view shows the slits across which the WS₂ was suspended. (d) SEM image of a suspended WS₂ device. The transferred WS₂ layer after cleaning remained coated in a thin layer of residual amorphous carbon.¹⁸ (e) Illustrations showing top and side views of the effect high-bias has on the WS₂ device.

The WS₂ devices were imaged prior to application of a high-bias, revealing the expected hexagonal lattice (Figure 2a). Application of a negative Fourier filter mask to the fast Fourier transform (FFT) of Figure 2a permitted reconstruction of the image without the WS₂ lattice contributions (Figure 2b), revealing the thin layer of amorphous carbon on the surface. We also demonstrated the presence of surface carbon residue by using the beam to induce a crack in the WS₂ in one of the devices (Figure 2c-g). The presence of this residue is a consequence of the film being freely suspended, with organic contaminants

from the environment readily anchoring themselves to the membrane. Heating the sample in activated carbon prior to experiments was used to remove the majority of the contamination.¹⁹

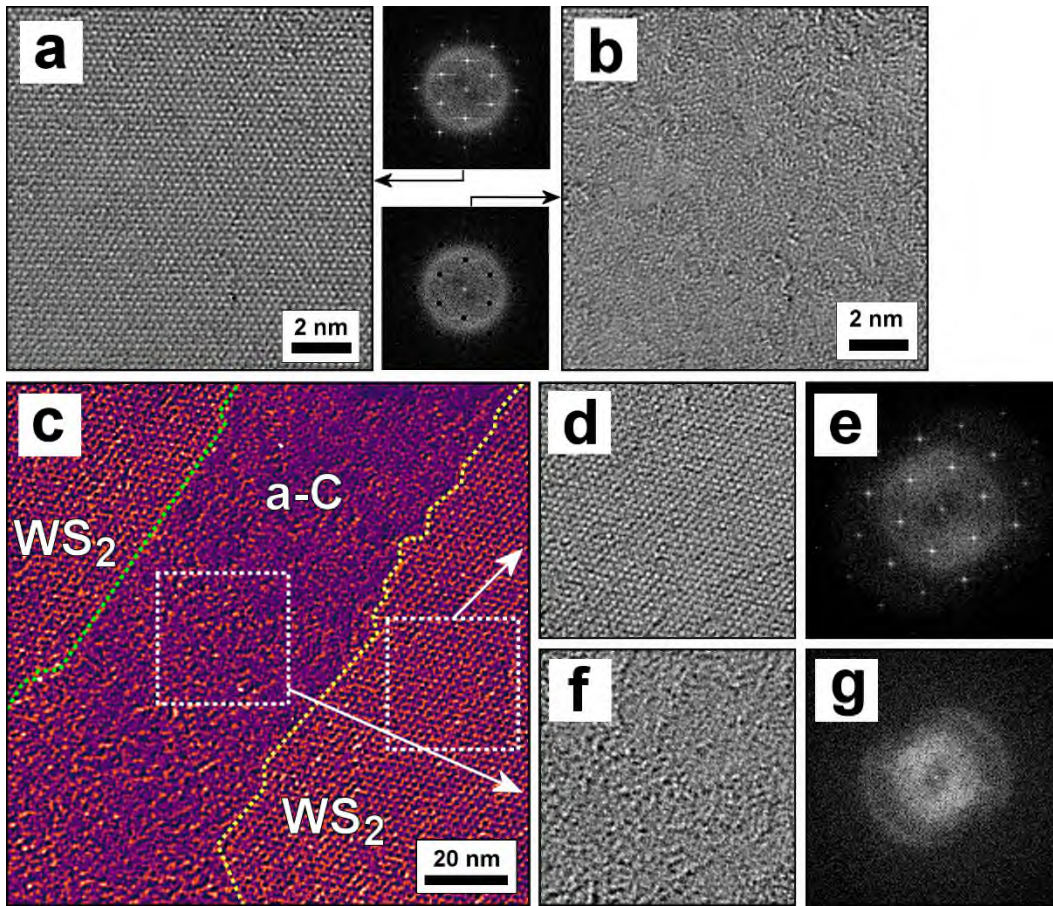


Figure 2. (a) AC-TEM image of monolayer WS₂ prior to breakdown, and (b) reconstructed image from a negatively masked FFT (insert) showing carbon surface residue. (c-g) AC-TEM images and accompanying FFTs of a monolayer WS₂ device with a beam induced crack (not used for breakdown experiments), showing amorphous carbon inside the crack.

In-situ characterization of the fabricated mono- and few-layer devices through sequential voltage sweeps demonstrated that there was some evolution in I-V behavior following biasing (Figure 3b and d). Such hysteresis has been frequently reported for MoS₂ devices,^{20–22} and has been recently attributed to surface carbon residue in a suspended MoS₂ device study.²³ We systematically increased the applied bias on our devices until WS₂ structural breakdown was achieved. Increasing the source-drain bias beyond a threshold level (~ 4.5 V for monolayer, ~ 8 V for few-layer) led to a rapid (< 0.2 s) and irreversible increase in the current carrying capacity of the device (Figure 3e and f). TEM imaging following the biasing revealed that for both mono- and few-layer devices the WS₂ layer between the electrodes was replaced by

turbostratic few-layer graphene decorated with nanoparticles (Figure 3g-j). The graphene did not uniformly fill the entire area between the two electrodes, with areas of vacuum also evident (Figure S2), but still formed a complete conductive pathway. Breakdown of the few-layer WS₂ also resulted in the formation of faceted tendrils along the breakdown vaporization edge of the remaining pristine WS₂ (Figure 3i and Figure S3), which was not observed in the monolayer devices (Figure 3g). A voltage sweep after breakdown demonstrated an order of magnitude increase in current density due to the formation of graphene (Figure 3k).

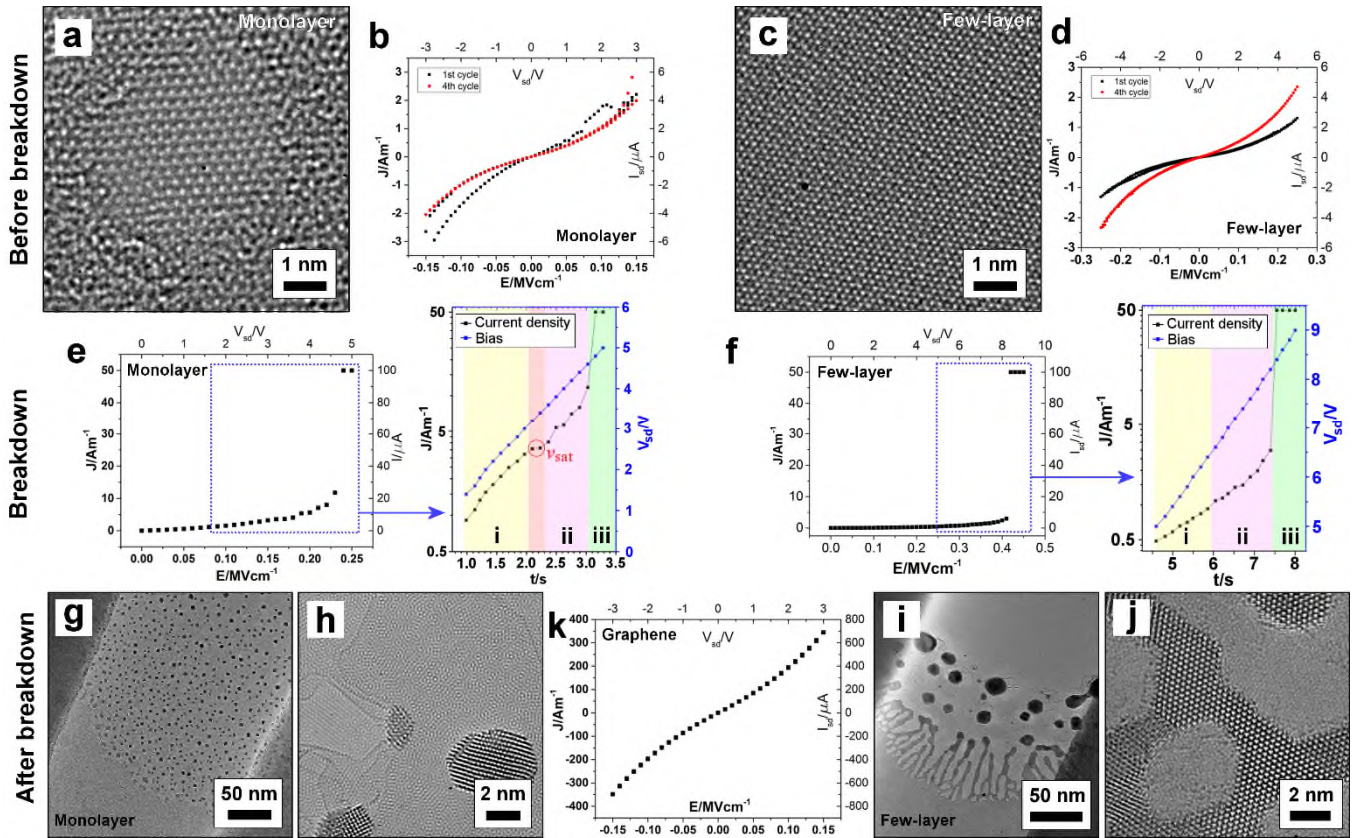


Figure 3. (a) AC-TEM image of monolayer WS₂ prior to high-bias, visible in a window in the surface residue. (b) Two I-V cycles of a WS₂ monolayer device. (c) AC-TEM image of a few-layer WS₂ device prior to high-bias. (d) Two I-V cycles of a WS₂ few-layer device. (e,f) High bias I-V plots leading to WS₂ disintegration for a (e) monolayer, and (f) few-layer device. Highlighted areas labelled i-iii are referenced in the main text. Magnified plots use a logarithmic scale for the current density. Data acquisition frequency is every 0.2 s. (g,h) AC-TEM images of a post high-bias monolayer sample, showing nanoparticles decorating a few-layer graphene surface. (i,j) AC-TEM images of a post high-bias few-layer sample, showing nanoparticle decorated graphene and tendrils along the breakdown interface. (k) I-V sweep performed after WS₂ breakdown, characteristic of graphene.

More detailed analysis of the high-bias plots in Figure 3e and f suggests different stages in device behavior as the source-drain bias was increased, labelled i-iii in the plots. During the low bias (i) regime the current increases constantly with the bias. At intermediate bias (ii) the rate of current increase escalates with voltage, and the dependence becomes more erratic. Decreasing the bias at this stage results in low hysteresis of the device behavior, *i.e.*, the effect is largely reversible. In the final high bias (iii) we observe a large, irreversible (Figure S4), increase in the current density. These stages share some resemblance to the (i) linear, (ii) soft breakdown, and (iii) hard breakdown regimes that are expected in a device. This correspondence is further supported by the observation of possible carrier saturation in the monolayer device (Figure 3e), labelled v_{sat} , occurring between stages (i) and (ii). Physically, the observation of these differing bias-dependent device behaviors would suggest different conduction modes. For instance, stage (i) likely corresponds to the standard linear conduction of the WS₂ layer, which in some devices can reach saturation when under sufficiently high bias. The observation of a sharper current increase in stage (ii) could be the result of Joule heating enabling improved conductivity through the amorphous carbon, permitting a greater contribution from this several atom thick layer in current flow. Amorphous solids conduct through a variable-range charge hopping mechanism, which in the case of amorphous carbon is hopping between localized band tail states of the sp^2 π orbitals.²⁴ An additional carrier excitation path becomes available above room temperature, laying closer to the mobility edge, thus increasing the conductivity further with escalating temperature.²⁵ This also explains the reversibility of this stage, as at lower biases the device would run cool and behavior would revert. The final stage (iii) represents the complete breakdown of the WS₂ layer, with an apparent simultaneous (less than 0.2 s) replacement by the graphitized amorphous carbon.

The formation of graphene and breakdown of the WS₂ must occur near-simultaneously; if the graphene formed prior then a boost in current density would be observed before breakdown and would effectively suppress the observation of carrier velocity saturation in the WS₂ (Figure 3e). Thus to explain the observed high-bias processes we require a mechanism that can explain both the WS₂ disintegration and the simultaneous graphitization.

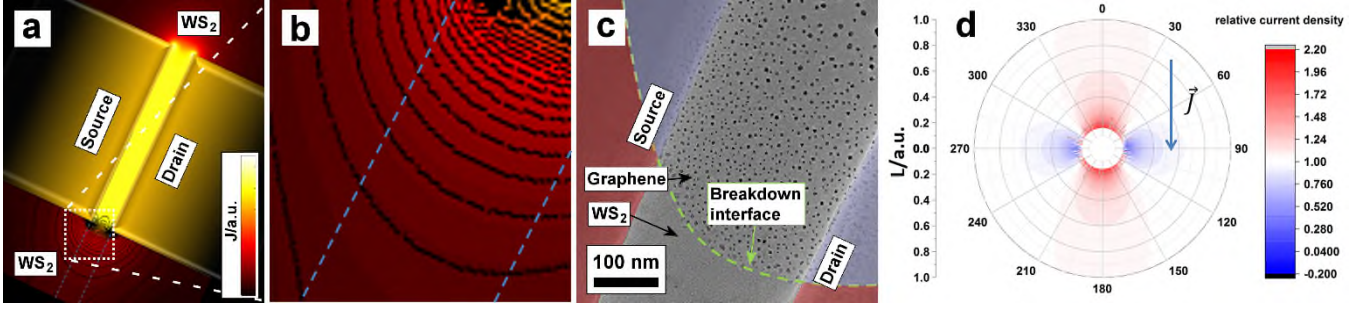


Figure 4. (a) Contour plot showing simulated current density distribution flowing through a WS₂ sheet spanning two electrodes. (b) Magnified view showing the contour lines of current density in the WS₂ beyond the end of the electrodes. Blue lines indicate the extension of the electrodes. (c) Low magnification TEM image of between the electrodes following bias-induced breakdown showing a curved breakdown interface between the high-bias formed graphene on one side and undamaged WS₂ on the other. The red/blue coloring of the electrodes suggest potential high/low contact resistance areas (see main text). (d) Simulated current density around a hole in WS₂ filled with graphene.

We modelled the current density passing through a WS₂ layer between two electrodes by solving the Poisson's equation (see Supporting Information). The contour plot of this current density profile is shown in Figure 4a, modeling a WS₂ sheet spanning between two electrodes and continuing on either side of the electrodes width. The current density through the WS₂ can be seen to decay with distance away from the inter-electrode gap, as shown with a series of curved contours in Figure 4b. This current density decay contour is reflected in the shape of the breakdown interface observed (Figure 4c, also see Figure 3i). In practice we found that the breakdown interfaces were not situated in the WS₂ beyond the electrodes, but at some point between them. We suggest this is potentially due to irregular contact resistance between the WS₂ and the electrode along the $\sim 1 \mu\text{m}$ electrode width; in this case the region of high current density is where there is good contact, and the breakdown interfaces occur at the where there is a high contact resistance segment of the electrode width. The similarity in the curvature of the breakdown interface to the model suggests that the disintegration of the WS₂ and the formation of graphene requires a critical current density. Combined with our observation of the carrier velocity saturation, this would suggest that the WS₂ undergoes an avalanche breakdown process.⁹ We observe velocity saturation at 0.13 MV cm^{-1} , in good agreement with other experiments for MoS₂.^{26,27} Avalanche breakdown occurs under these high electric fields, where the carrier acceleration is sufficient to reach velocities that permit ionization and the

generation of secondary charges, so-called hot carriers. These can then generate further hot carriers in additional impact ionizations in a runaway avalanche effect, which typically leads to a massive increase in device current. However, in a suspended two-dimensional material the depopulation of electrons from the valence band would likely lead to weakening and breaking of bonds during these impact ionizations, and thus disintegrate the WS₂.

Alternatively, the high current density could raise the temperature above 1,250 °C, the decomposition temperature of WS₂, through Joule heating. This would also explain the simultaneous graphitization process, which has been shown to occur at temperatures of 1,500 °C.²⁸ To reach these high temperatures we suggest that rather than the entire film being subjected to a uniform current density between the electrodes, as suggested in Figure 4a, that instead defects and impurities could lead to localized nanoscale regions of very high current density and heating. These would lead to the formation of small islands of graphene. The excellent conductivity of graphene compared to the surrounding WS₂ would focus the electric field through these areas, amplifying the current density in the adjacent WS₂ regions (Figure 4d) and thus the propagation of the Joule heating front through the film.

We now move to discuss the formation of the breakdown products; confirmation of the formation of graphene, identification of the nanoparticles, and characterization of the WS₂ vaporization/breakdown boundary.

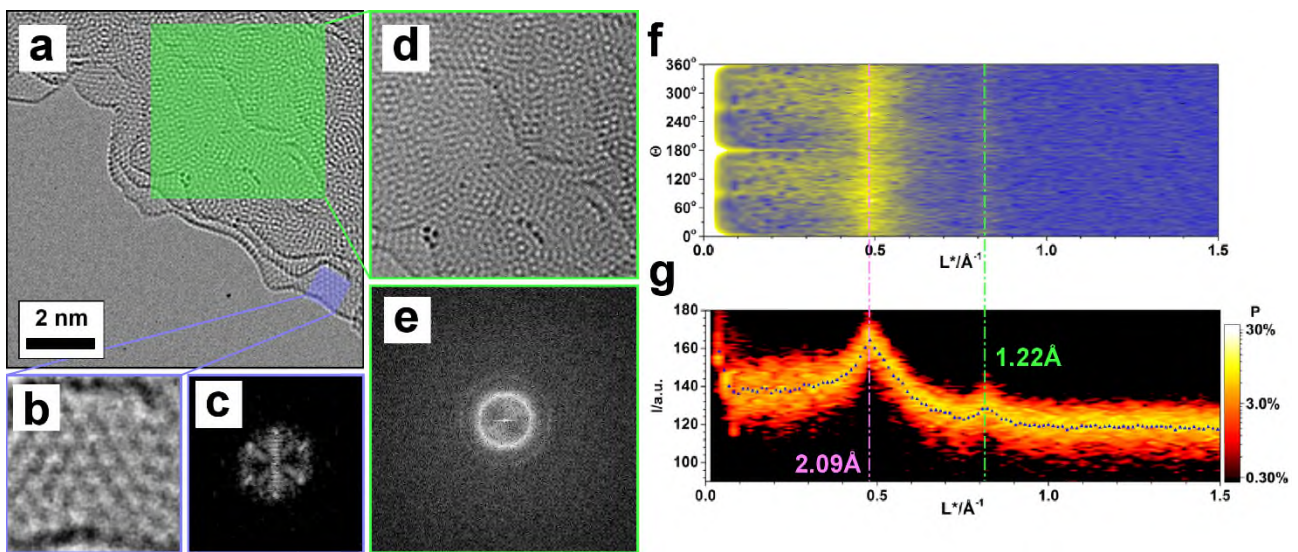


Figure 5. Characterization of the post-WS₂ breakdown graphene. (a) AC-TEM image taken from the edge of the few-layer graphene. (b) Magnified view of a graphene monolayer, showing the expected lattice as confirmed by a fast Fourier transform (FFT) in (c). (d,e) Magnified view and FFT of the turbostratic few-layer graphene area. (f)

Polar co-ordinate transform of the FFT of the post WS₂ breakdown graphene, (g) with integration revealing the expected {100} and {110} peaks at 2.09 Å and 1.22 Å.

Confirmation that the formed layered material was well crystallized graphene was obtained through high magnification AC-TEM imaging. Figure 5a shows the edge of a few-layer graphene film, with a magnified view of a monolayer edge demonstrating the expected hexagonal lattice (Figure 5b) and FFT reflections (Figure 5c) associated with graphene. The few-layer areas exhibit moiré patterns (Figure 5d), arising either from the graphitization process yielding only small graphene grains with no inter-layer correlation, and/or as a result of the graphene tearing apart during breakdown to fold-in on itself. Using a wider area for forming the FFT allows us to accurately measure lattice reflections (Figure 5e-g), confirming that they correspond to that expected from graphene.

Closer inspection of the nanoparticles revealed the formation of several different types. Well-defined cubic nanoparticles were observed (Figure 6a-c), some of which exhibited good faceting. Analysis of a combined polar transform (see methods) FFT of these particles show reflections in good agreement with that expected of BCC W (Figure 6d). Other well-crystallized particles with hexagonal symmetry were observed (Figure 6e-g), with the summed FFT showing inner reflections at 2.7 Å (Figure 6h), in good agreement with the reflections expected from WS₂. These show that breakdown of WS₂ and the subsequent film disintegration does not necessarily lead to the complete evolution of the constituent atoms to vapor, but rather the WS₂ layer disintegrates with some re-assembling in to W and WS₂ nanoparticles. Unfortunately confirmation of the chemical identity of the nanoparticles by energy dispersive X-ray spectroscopy (EDS) was not possible due to the geometry of the *in-situ* holder tip, which blocked the detector. However, beyond the imaging and FFT evidence, our assessment that many of the nanoparticles are made of W and WS₂ is further supported by considering the nanoparticle size. Analysis of the particle size distribution for both post-breakdown mono- and few-layer WS₂ devices shows a marked increase in mean particle diameter for the few-layer case, from 4.4 nm to 9.9 nm (Figure S5). We propose that this is related to the increased supply of W and S available in the few-layer system.

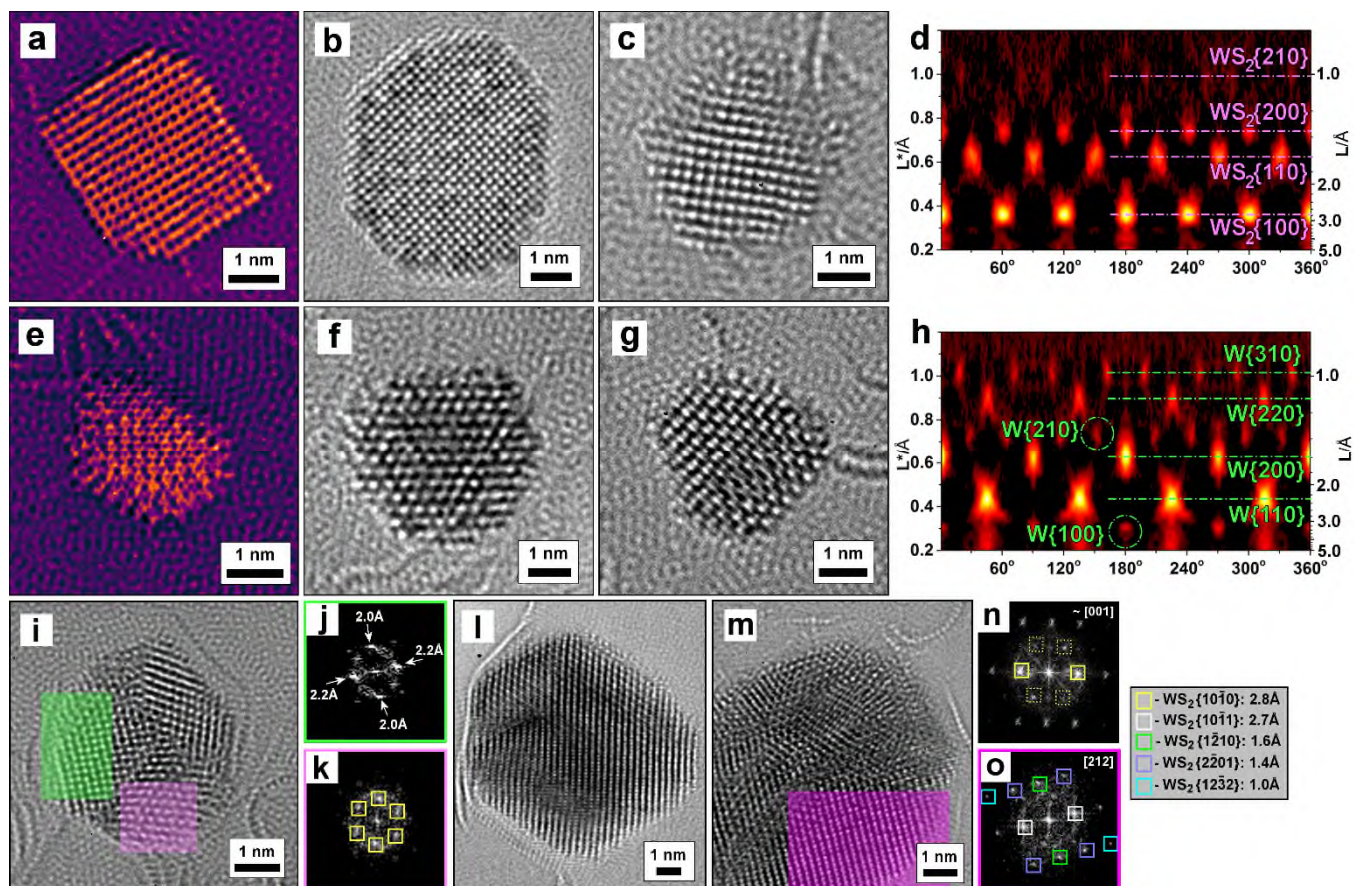


Figure 6. W and WS₂ nanoparticles on graphitized carbon after WS₂ high-bias disintegration. (a-c) Representative AC-TEM images of W nanoparticles found post-WS₂ breakdown. (d) Averaged FFT (polar coordinates) of all W nanoparticles, with dashed lines showing the {110} and {200} reflections of W at $r = 2.2$ Å and $r = 1.8$ Å. (e-g) Representative AC-TEM images of WS₂ nanoparticles formed post-breakdown. (h) Averaged FFTs (polar coordinates) of all WS₂ nanoparticles, represented in polar coordinates, showing the {100} reflections of WS₂ at $r = 2.7$ Å. (i-k) AC-TEM image and accompanying FFTs from corresponding colored areas, showing a distorted cubic structure (2.0 and 2.2 Å reflections) interfaced with a grain corresponding to WS₂ viewed down the [001] axis. (l, m) AC-TEM images of larger nanoparticles from few-layer WS₂ breakdown. (n, o) FFTs from the entire nanoparticle in (l) and the shaded area in (m), respectively, exhibiting reflections corresponding to WS₂ viewed down the \sim [001] and [212] axes, respectively.

Accompanying these regular nanoparticles were numerous polycrystalline particles (Figure 6i, l, m). Analysis of FFTs extracted from these particles suggest that they are defective WS₂. We have checked across our dataset for matches to any of the expected lattice reflections and symmetries from various W_xC_y compounds,²⁹ however none were found. Many of these particles possessed crystal twinning and dislocation defects and were less likely to exhibit clean faceting. The WS₂ particle in Figure 6i was

observed to exhibit a crystal grain with an orthorhombic structure (Figure 6j), which directly interfaced with the WS₂ grain. We suggest that this is a highly S depleted WS₂ grain, formed due to preferential S vaporization during breakdown, which shall be discussed further later (Figure 8).

A notable difference in the breakdown of the mono- and few-layer WS₂ devices is the structure of the vaporization boundary, with the few-layer devices yielding additional faceted tendril structures along the curved boundary (Figure 7b and c). The tendrils possessed a high density of line defects, indicated with blue arrows in Figure 7d and e and leading to blurred or split reflections in the FFTs. Comparison of the lattice structure of the tendrils reveals instances of cubic and orthorhombic symmetry, which interface directly with the majority WS₂ structure (Figure 7d and f, black arrows). A cubic instance shown in Figure 7d exhibits reflections at 2.2 Å, corresponding to the expected {110} reflections for BCC W. An orthorhombic atomic interface is shown in Figure 7f, black arrow, which we identify as strained W, and is explored further in Figure 8. The interface between tendril and the bulk (Figure 7f, white arrow) exhibit epitaxial matching. However it is apparent from this image, and from low magnification images of the boundary (Figure 7g), that the contrast of the tendrils are somewhat darker than the pristine WS₂. A box averaged intensity profile across the interface (Figure S6) confirms the contrast with respect to the vacuum is 1.5 times greater for the edge area than the bulk.

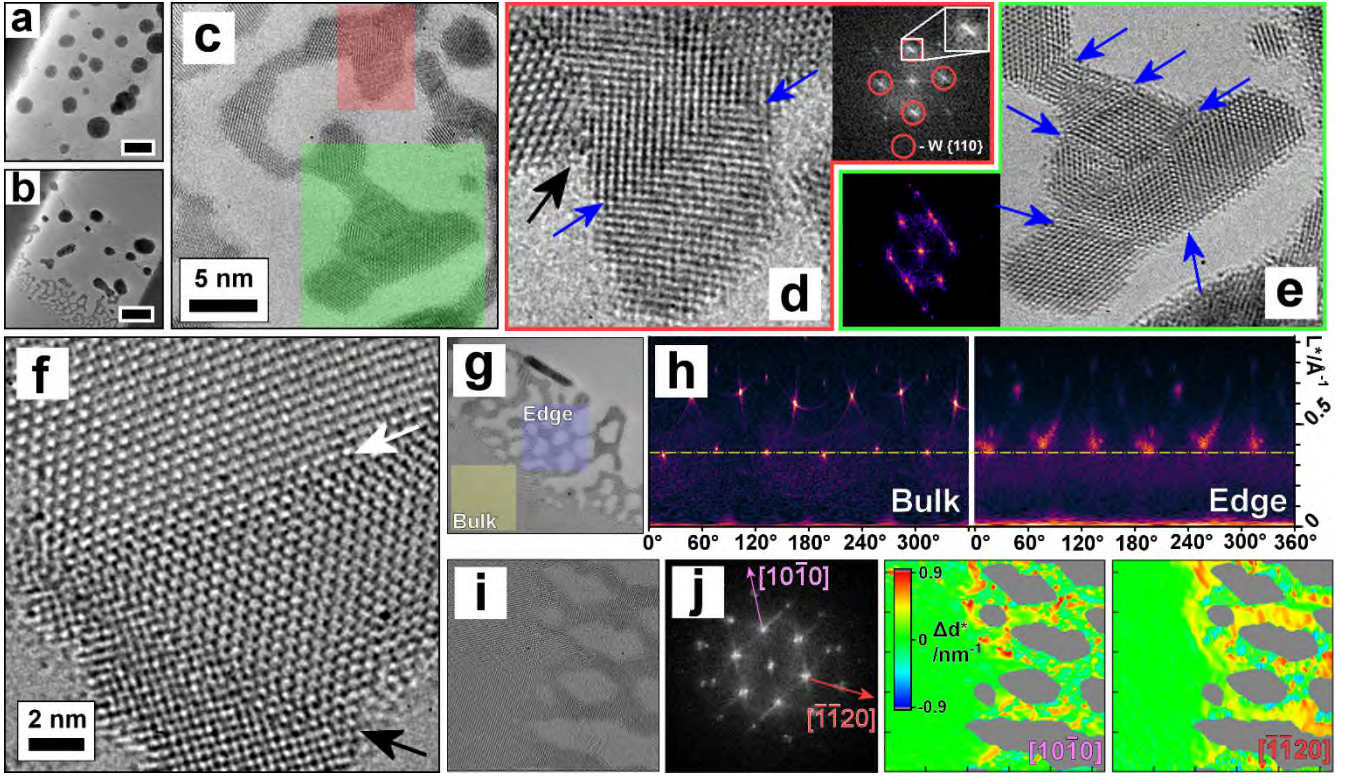


Figure 7. High bias disintegration of few-layer WS₂. (a) Low magnification TEM image of nanoparticle decorated graphene post-breakdown. Scale bar 20 nm. (b) Low and (c) high magnification images showing faceted W and WS₂ structures at the vaporization boundary. (d,e) Magnified views from shaded areas in (c), alongside FFTs. Blue arrows indicate line defects. Black arrow indicates W-WS₂ interface. (f) AC-TEM image of the interface between pristine WS₂ and tendrils (white arrow) and W-WS₂ interface (black arrow). (g) Wide-field view of a vaporization boundary. (h) Polar coordinate FFTs taken from the shaded areas in (g), corresponding to the pristine bulk and the tendrils edge. The line annotation is for $r = 2.77 \text{ \AA}$. (i) TEM image of tendrils/bulk interface and (j) maps of the deviation (Δd^*) of indicated $\{100\}$ reflections along the $[10-10]$ and the $[-1-120]$ axis, respectively.

Possible explanations for the darker contrast are either that the tendrils comprise more layers, or the lattice is more densely packed (*i.e.*, compressed). To explore the latter possibility we systematically characterized the FFTs of all the edge tendrils in comparison to the pristine bulk areas in our dataset to identify any lattice contraction. This analysis demonstrated the lattice in the tendrils had undergone an average contraction of $(7.3 \pm 1.5)\%$ compared to the pristine WS₂. An example of this analysis is shown in Figure 7g and h, showing polar coordinate FFTs acquired from the indicated areas of the TEM image of a vaporization boundary. The dashed line indicates the average radial distance of the WS₂ $\{100\}$ reflections in the pristine bulk area, which lies beneath the equivalent reflections in the polar FFT acquired from the edge area, indicating a 4.7% contraction in the lattice in this instance. Research in the literature

on RF sputtered MoS₂, which is typically S deficient, has shown a similar contraction in the basal lattice,^{30,31} and a more recent atomic resolution AC-TEM study demonstrated that contraction can arise due to the formation of linear chains of S vacancies, or S vacancy lines (SVLs).³² This is supported by the observation of extensive line defects in our tendril structures. Further evidence that the observed contraction is due to S depletion of the WS₂ is illustrated by mapping the deviation in the WS₂ {100} reflections across the breakdown interface (Figure 7i and j). These maps reveal that the lattice contraction is limited to the tendrils and is non-uniform. This range of localized contractions is attributable to the irregular distribution of S vacancies across the tendrils.

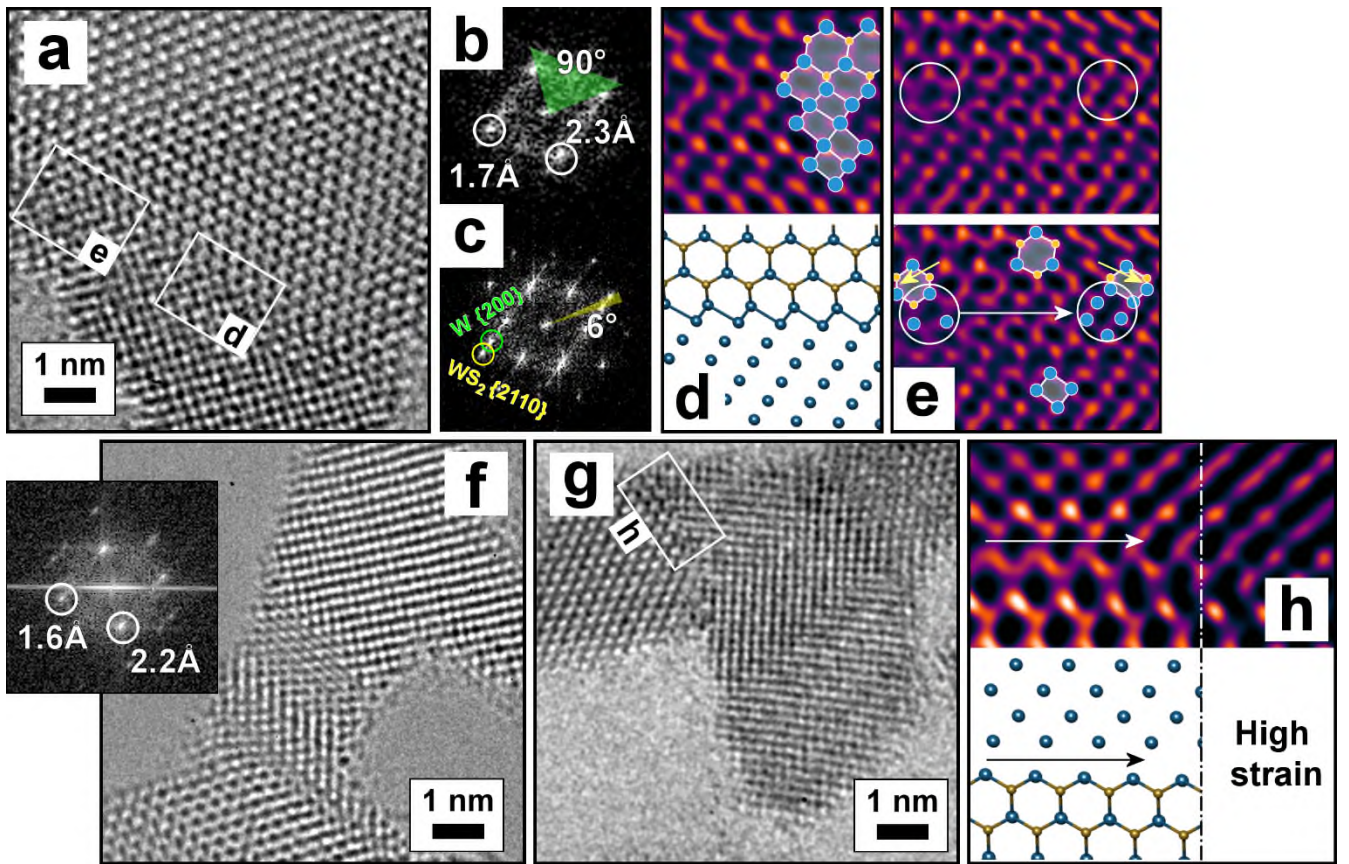


Figure 8. (a) AC-TEM image of the W-WS₂ interface, as in Figure 7f. (b) FFT from the W lattice in (a) viewed down the [110] axis. The {111} and {200} reflections suggest moderate lattice expansion from pristine W. (c) FFT from across the entire tendril in (a), showing a 6° rotational misalignment between the W and WS₂ lattices. (d) Magnified view of the indicated area in (a), and accompanying atomic model, showing the atomic structure of the W-WS₂ interface. (e) Magnified view of the indicated area in (a), and accompanying annotated image, showing a shift in interface structure. (f) A W-WS₂ interface, with W viewed down the [110]. The insert FFT shows the W lattice is pristine. (g) A W-WS₂ interface, as shown in Figure 7d, viewing W down the [001] axis. (h) Magnified view of the interface indicated in (g), showing the atomic structure of the interface and shift toward high strain.

Figure 7f **Figure 7** shows an atomic interface between the hexagonal WS₂ and an orthorhombic structure (black arrows). More detailed characterization of Figure 7f is presented in Figure 8, with Figure 8a showing a magnified view of the interface. Examination of the lattice structure by acquiring FFTs (Figure 8b and c) demonstrates that the orthorhombic lattice is likely distorted W viewed down the [110] axis. Reflections for pristine W are expected at $\{110\} = 2.2 \text{ \AA}$ and $\{200\} = 1.6 \text{ \AA}$, suggesting that the W lattice is moderately expanded. As discussed above (Figure 7h), the WS₂ lattice in the tendrils also exhibit evidence of contraction. These respected distortions to the crystal lattices enable good crystal structure matching across the W-WS₂ interface, as demonstrated by atomic resolution imaging (Figure 8d). The accompanying atomic model sketch uses a WS₂ lattice with unit cell parameter $a = 2.93 \text{ \AA}$, as per the 7.3% contraction from 3.15 \AA measured in Figure 7, and W of $a = 3.3 \text{ \AA}$, a 4.4% expansion that agrees with that measured in Figure 8b. This model shows good agreement with the AC-TEM image, and illustrates how the lattices can have epitaxy following distortion; pristine W and WS₂ lattices would not exhibit such epitaxy (Figure S7). In Figure 8e the start of the W-WS₂ interface line shows the shift in the lattice necessary to accommodate the pristine WS₂ lattice on the tendril edge. Annotations indicate this shift from hexagonal WS₂ to the orthorhombic W, accommodated by a gradual decrease in the apparent W-S bond length orthogonal to the interface in the WS₂ unit cells immediately along the interface edge (yellow arrows). This apparent W-S bond length contraction is likely due to S atom removal, permitting the W atom to buckle under the adjacent S, as in sulfur vacancy lines reported previously.³² A further similar example of a W-WS₂ interface was observed that did not exhibit the same expansion in the W lattice (Figure 8f); here we see the expected 2.2 \AA and 1.6 \AA reflections in the FFT. However, it can be seen that there is no clear atomic interface between the orthorhombic W lattice at the top of the image and the hexagonal WS₂ lattice toward the bottom, with instead a more complex extended interface connecting the two. Interfaces between W (100) and WS₂ were also observed (Figure 8g), however it can be seen that this does not exhibit good epitaxy, with a rapid shift along the interface toward a disordered region (Figure 8h). This is a consequence of the contraction of the WS₂ lattice in the tendrils (Figure S8).

Conclusion

The electric breakdown of suspended WS₂ mono- and few-layer films has been studied *via in-situ* TEM. We demonstrate that the disintegration of the WS₂ film at high electric fields is accompanied by the formation of graphitized sheets, formed from the thin amorphous carbon residue on the WS₂. The observed W phases in the tendrils, alongside the observation of defective nanoparticles (Figure 6) and extensive line defects and lattice contraction near the disintegration interface (Figure 7), suggest the disintegration of the WS₂ layer during high-bias occurs through the preferential release of S. The combination of observing graphitization and preferential S vaporization suggests a thermal rather than avalanche breakdown mechanism. Atomic imaging revealed the bonding interface between the WS₂ and W grains, with the quality of the epitaxy strongly influenced by the contracted lattice in the S depleted WS₂ remnant.

Methods

TEM Imaging and Analysis

Imaging was performed on Oxford's JEOL 2200MCO AC-TEM at 80 kV. Images were subjected to a 2 pixel Gaussian blur to remove noise and aid image interpretation. FFTs have sometimes been displayed in polar coordinates for clarity. We used the Polar Transformer plugin for ImageJ to achieve this (<https://imagej.nih.gov/ij/plugins/polar-transformer.html>). Atomic resolution images have been subject to stigmatism correction post-processing where possible, as outlined in ref. [33]. In brief, an FFT was acquired from the WS₂ lattice of the image to be corrected. The six reflections were fitted to an ellipse,³⁴ with semi-major and semi-minor axes that describes the degree of astigmatism in the image, as well as a rotation angle. The real-space image was then rotated so the x and y axes corresponded to the major and minor axes, and subjected to appropriate x and y scaling factors to correct for this astigmatism.

Calibration

The lattice parameter of pre-breakdown WS₂, and graphene reference samples, were used to calibrate the high-mag TEM data. The unit cell parameter of WS₂ was taken as 0.3158 nm, and graphene as 0.2462 nm. To avoid any local effect due to residual lens aberrations the calibration was carried out by averaging all of the same family of reflections measured in the FFT.

Fabrication of the Si/SiN Chip

Si wafers (p-doped, 200 μm thick, 4" diameter) were first subjected to a RCA clean. The Si-rich SiN thin film (100 nm thick) was deposited on both sides of the cleaned Si wafers through low-pressure chemical vapor deposition (LPCVD). During deposition the substrate temperature is fixed at 850 $^{\circ}\text{C}$ and the gas ratio between SiH_2Cl_2 and NH_3 is maintained at 100:25. The view window was patterned by photolithography on one side of the SiN, then etched by reactive ion etching. SiN inside of the observation window was etched by wet etching (45% w/w KOH solution at 80 $^{\circ}\text{C}$), leaving a suspended SiN film across the observation window.

WS₂ Synthesis and Transfer

Details and diagrams for the procedure are in ref. [14]. A double walled quartz tube was inserted through two tube furnaces. S precursor powder (300 mg 99.5%) was placed in the outer tube and aligned with the first furnace. WO_3 (200 mg 99.9%) precursor was inserted into the inner tube within the second CVD tube furnace, at the center of the hot-zone of the furnace and the substrate (Si/SiO₂ chip) was located in the outer tube with a pre-calibrated distance further downstream. Ar carrier gas was used to bring reactant vapor to the substrate, permitting WO_3 sulfurization at the substrate. The first, S containing, furnace was held at 180 $^{\circ}\text{C}$, and the second furnace at 1170 $^{\circ}\text{C}$, with the reaction stage taking 3mins. Samples were rapidly cooled by removal from the furnace following the reaction stage.

Transfer was achieved by spin-coating the sample with a supporting PMMA scaffold (8% wt., m_w 495k). The PMMA/WS₂ stack was separated from the SiO₂/Si substrate by KOH etching (1 M) at 60 $^{\circ}\text{C}$. The PMMA/WS₂ film was transferred *via* clean glass slides to deionized water to rinse residue from the WS₂ side, which was repeated several times. The film was then transferred to sample chip, allowed to dry overnight, and then heated on a hot plate at 150 $^{\circ}\text{C}$ to drive off remaining water and promote sample adhesion.

WS₂ Device Patterning and Fabrication

The chips were patterned by electron beam lithography using a JEOL JBX-5500FS, followed by metallization and lift-off. The patterned electrodes were aligned with the viewing window by imaging the sample within the JBX-5500FS, and then appropriately positioning the pattern relative to pre-patterned

alignment markers. The contacts were metalized by thermal evaporation of 90 nm Au with a 10 nm Cr adhesion layer. The suspended region was then created by bisecting the contacts by focused ion beam milling (Zeiss NVision) of a ~ 200 nm slit through both the metal contacts and the suspended SiN film, yielding a source-drain electrode separated by vacuum. Sets of three devices on each chip share a common ground/drain. Following WS₂ transfer to the chip the chip was wire bonded to a custom PCB that can be clamped in the biasing TEM holder.

Cleaning

Following the transfer of WS₂ to the device and PMMA removal *via* solvent rinsing the chip was buried in activated carbon and heated. The temperature was set to 200 °C and the sample was heated for 2 hours.

The Supporting Information is available free of charge on the ACS Publications website at DOI: 10.1021/acsnano.xxxxxxx. Further TEM images of post-breakdown devices, PL and Raman spectra of WS₂, size distributions of formed nanoparticles, intensity/contrast measurements across the breakdown film, solving of the Poisson's equation, and illustrative atomic models, as referenced in the main text.

Acknowledgements

Y.F. is thankful for the support from the Clarendon Scholarship from the University of Oxford. J.H.W. thanks the Royal Society for support. A.W.R. has been supported by EPSRC (Platform Grant EP/K032518/1). MHR thanks the National Science Foundation China (NSFC. Project 51672181) and the National Science Center within the frame of the Opus program (Grant agreement 2015/19/B/ST5/03399). Aspects of this work (image analysis) were supported by the Chemical Imaging Initiative, a Laboratory Directed Research and Development Program at Pacific Northwest National Laboratory (PNNL). PNNL is a multi-program national laboratory operated by Battelle for the U.S. Department of Energy (DOE) under Contract DE-AC05-76RL01830.

Reference

- (1) Novoselov, K. S.; Fal'ko, V. I.; Colombo, L.; Gellert, P. R.; Schwab, M. G.; Kim, K. A Roadmap

for Graphene. *Nature* **2012**, *490*, 192–200.

- (2) Radisavljevic, B.; Radenovic, A.; Brivio, J.; Giacometti, V.; Kis, A. Single-Layer MoS₂ Transistors. *Nat. Nanotechnol.* **2011**, *6*, 147–150.
- (3) Gong, Y.; Lin, J.; Wang, X.; Shi, G.; Lei, S.; Lin, Z.; Zou, X.; Ye, G.; Vajtai, R.; Yakobson, B. I.; Terrones, H.; Terrones, M.; Tay, B. K.; Lou, J.; Pantelides, S. T.; Liu, Z.; Zhou, W.; Ajayan, P. M. Vertical and in-Plane Heterostructures from WS₂/MoS₂ Monolayers. *Nat. Mater.* **2014**, *13*, 1135–1142.
- (4) Bessonov, A. A.; Kirikova, M. N.; Petukhov, D. I.; Allen, M.; Ryhänen, T.; Bailey, M. J. A. Layered Memristive and Memcapacitive Switches for Printable Electronics. *Nat. Mater.* **2014**, *14*, 199–204.
- (5) Kang, K.; Xie, S.; Huang, L.; Han, Y.; Huang, P. Y.; Mak, K. F.; Kim, C.-J.; Muller, D.; Park, J. High-Mobility Three-Atom-Thick Semiconducting Films with Wafer-Scale Homogeneity. *Nature* **2015**, *520*, 656–660.
- (6) Fiori, G.; Bonaccorso, F.; Iannaccone, G.; Palacios, T.; Neumaier, D.; Seabaugh, A.; Banerjee, S. K.; Colombo, L. Electronics Based on Two-Dimensional Materials. *Nat. Nanotechnol.* **2014**, *9*, 768–779.
- (7) Klein, N. Electrical Breakdown in Solids. *Adv. Electron. Electron Phys.* **1969**, *26*, 309–424.
- (8) Zener, C. A Theory of the Electrical Breakdown of Solid Dielectrics. *Proc. R. Soc. A Math. Phys. Eng. Sci.* **1934**, *145*, 523–529.
- (9) Mahadevan, S.; Hardas, S. M.; Suryan, G. Electrical Breakdown in Semiconductors. *Phys. Status Solidi* **1971**, *8*, 335–374.
- (10) Hattori, Y.; Taniguchi, T.; Watanabe, K.; Nagashio, K. Layer-by-Layer Dielectric Breakdown of Hexagonal Boron Nitride. *ACS Nano* **2015**, *9*, 916–921.
- (11) Lembke, D.; Kis, A. Breakdown of High-Performance Monolayer MoS₂ Transistors. *ACS Nano* **2012**, *6*, 10070–10075.
- (12) Yu, J.; Liu, G.; Sumant, A. V.; Goyal, V.; Balandin, A. A. Graphene-on-Diamond Devices with Increased Current-Carrying Capacity: Carbon sp²-on-sp³ Technology. *Nano Lett.* **2012**, *12*, 1603–1608.

- (13) Zhu, W.; Low, T.; Lee, Y.-H.; Wang, H.; Farmer, D. B.; Kong, J.; Xia, F.; Avouris, P. Electronic Transport and Device Prospects of Monolayer Molybdenum Disulphide Grown by Chemical Vapour Deposition. *Nat. Commun.* **2014**, *5*, 3087.
- (14) Rong, Y.; Fan, Y.; Leen Koh, A.; Robertson, A. W.; He, K.; Wang, S.; Tan, H.; Sinclair, R.; Warner, J. H. Controlling Sulphur Precursor Addition for Large Single Crystal Domains of WS₂. *Nanoscale* **2014**, *6*, 12096–12103.
- (15) Tan, H.; Fan, Y.; Zhou, Y.; Chen, Q.; Xu, W.; Warner, J. H. Ultrathin 2D Photodetectors Utilizing Chemical Vapor Deposition Grown WS₂ With Graphene Electrodes. *ACS Nano* **2016**, *10*, 7866–7873.
- (16) Gutiérrez, H. R.; Perea-López, N.; Elías, A. L.; Berkdemir, A.; Wang, B.; Lv, R.; López-Urías, F.; Crespi, V. H.; Terrones, H.; Terrones, M. Extraordinary Room-Temperature Photoluminescence in Triangular WS₂ Monolayers. *Nano Lett.* **2013**, *13*, 3447–3454.
- (17) Fan, Y.; Robertson, A. W.; Zhang, X.; Tweedie, M.; Zhou, Y.; Rummeli, M. H.; Zheng, H.; Warner, J. H. Negative Electro-Conductance in Suspended 2D WS₂ Nanoscale Devices. *ACS Appl. Mater. Interfaces* **2016**.
- (18) Ricolleau, C.; Le Bouar, Y.; Amara, H.; Landon-Cardinal, O.; Alloyeau, D. Random vs Realistic Amorphous Carbon Models for High Resolution Microscopy and Electron Diffraction. *J. Appl. Phys.* **2013**, *114*.
- (19) Algara-Siller, G.; Lehtinen, O.; Turchanin, A.; Kaiser, U. Dry-Cleaning of Graphene. *Appl. Phys. Lett.* **2014**, *104*, 153115.
- (20) Late, D. J.; Liu, B.; Matte, H. S. S. R.; Dravid, V. P.; Rao, C. N. R. Hysteresis in Single-Layer MoS₂ Field Effect Transistors. *ACS Nano* **2012**, *6*, 5635–5641.
- (21) Ghatak, S.; Pal, A. N.; Ghosh, A. Nature of Electronic States in Atomically Thin MoS₂ Field-Effect Transistors. *ACS Nano* **2011**, *5*, 7707–7712.
- (22) Li, T.; Du, G.; Zhang, B.; Zeng, Z. Scaling Behavior of Hysteresis in Multilayer MoS₂ Field Effect Transistors. *Appl. Phys. Lett.* **2014**, *105*, 93107.
- (23) Shu, J.; Wu, G.; Guo, Y.; Liu, B.; Wei, X.; Chen, Q. The Intrinsic Origin of Hysteresis in MoS₂

Field Effect Transistors. *Nanoscale* **2016**, 8, 3049–3056.

- (24) Robertson, J.; O'Reilly, E. P. Electronic and Atomic Structure of Amorphous Carbon. *Phys. Rev. B* **1987**, 35, 2946–2957.
- (25) Dasgupta, D.; Demichelis, F.; Tagliaferro, A. Electrical Conductivity of Amorphous Carbon and Amorphous Hydrogenated Carbon. *Philos. Mag. Part B* **1991**, 63, 1255–1266.
- (26) Fiori, G.; Szafrank, B. N.; Iannaccone, G.; Neumaier, D. Velocity Saturation in Few-Layer MoS₂ Transistor. *Appl. Phys. Lett.* **2013**, 103, 233509.
- (27) Liu, H.; Neal, A. T.; Ye, P. D. Channel Length Scaling of MoS₂ MOSFETs. *ACS Nano* **2012**, 6, 8563–8569.
- (28) Barreiro, A.; Börrnert, F.; Avdoshenko, S. M.; Rellinghaus, B.; Cuniberti, G.; Rummeli, M. H.; Vandersypen, L. M. K. Understanding the Catalyst-Free Transformation of Amorphous Carbon into Graphene by Current-Induced Annealing. *Sci. Rep.* **2013**, 3, 1115.
- (29) Kurlov, A. S.; Gusev, A. I. Phase Equilibria in the W–C System and Tungsten Carbides. *Russ. Chem. Rev.* **2006**, 75, 617–636.
- (30) Lince, J. R.; Fleischauer, P. D. Crystallinity of Rf-Sputtered MoS₂ Films. *J. Mater. Res.* **1987**, 2, 827–838.
- (31) Hilton, M. R.; Fleischauer, P. D. TEM Lattice Imaging of the Nanostructure of Early-Growth Sputter-Deposited MoS₂ Solid Lubricant Films. *J. Mater. Res.* **1990**, 5, 406–421.
- (32) Wang, S.; Lee, G.-D.; Lee, S.; Yoon, E.; Warner, J. H. Detailed Atomic Reconstruction of Extended Line Defects in Monolayer MoS₂. *ACS Nano* **2016**, 10, 5419–5430.
- (33) Robertson, A. W.; Lee, G.-D.; He, K.; Gong, C.; Chen, Q.; Yoon, E.; Kirkland, A. I.; Warner, J. H. Atomic Structure of Graphene Subnanometer Pores. *ACS Nano* **2015**, 9, 11599–11607.
- (34) Fitzgibbon, A.; Pilu, M.; Fisher, R. B. Direct Least Square Fitting of Ellipses. *IEEE Trans. Pattern Anal. Mach. Intell.* **1999**, 21, 476–480.

ToC Graphic

